Giant earthquakes on quiet faults governed by rheological transitions

Martijn P.A. van den Ende*, Jianye Chen, Jean-Paul Ampuero and André R. Niemeijer

The apparent stochastic nature of earthquakes poses major challenges for earthquake forecasting attempts. Physical constraints on the seismogenic potential of major fault zones may greatly aid in improving seismic hazard assessments, but the mechanics of earthquake nucleation and rupture are obscured by the enormous complexity that natural faults display. In this study, we investigate the mechanisms behind giant earthquakes by employing a microphysically based seismic cycle simulator. This microphysical approach is directly based on the mechanics of friction as inferred from laboratory tests, and can explain a broad spectrum of fault slip behaviour. We show that exceptionally large, fault-spanning earthquakes are governed by different micro-scale mechanisms than regular (small) earthquakes. More importantly, the stress-driven transition from ductile creep to granular flow facilitates the nucleation of giant earthquakes on faults that are otherwise seismically quiet. This microphysically based approach offers new opportunities for investigating long-term seismic cycle behaviour of natural faults.

One major limitation of seismic hazard assessments is that they are mostly based on statistics rather than physics. Particularly for large earthquakes that have recurrence times of up to several centuries, instrumental catalogues of seismic events in a given region are short or absent, so that statistical analyses can only be performed through the extrapolation of smaller, more frequent events, which entails model assumptions that are difficult to test. Constraints originating from a physical understanding of earthquakes may therefore greatly improve seismic hazard assessments, but basic underlying mechanisms are obscured by the enormous complexity inherent to natural fault zones.

Over the last two decades or so, innovative techniques in palaeoseismology have substantially expanded our catalogue of (pre)historic seismic events, revealing spatio-temporal clustering of earthquakes [1–4] and occurrences of exceptionally large events ('superimposed cycles') [5–8]. In addition, millenary recurrence of $M_w \geq 9.0$ earthquakes has been anticipated for the Main Himalayan Thrust [9] and Japan Trench [10] regions on the basis of geodetic estimates of moment accumulation rates. These inferences suggest that the lack of instrumental recordings of great ($M_w > 8$) and giant ($M_w > 9$) earthquakes does not imply an intrinsic upper limit of event magnitude. The 2004 Sumatra-Andaman and 2011 Tohoku-Oki $M_w > 9$ events, hosted by subduction thrusts that were previously marked as being incapable of generating such large magnitude events [10–12], are exemplary to this notion. Statistical analyses of earthquake catalogues do not exclude that most (if not all) subduction regions are intrinsically capable of hosting giant earthquakes [13,14], provided that the seismogenic zone geometry is not restrictive (e.g. Weng & Yang [15]).

The seemingly universal appearance of great earthquakes in subduction settings is suggestive of a common underlying mechanism. On the other hand, though numerous subduction regions have been identified to host giant earthquakes, some of these regions presently exhibit high seismicity rates (Japan Trench[8], Sumatra[4]), while other megathrusts are currently quiescent except for deeper slow slip and tremor (Alaska[16], Cascadia[17]), or generally display low levels of background seismicity (Andaman, Chile Maule[18]). This geographical variability in seismic character requires that the mechanism for the generation of giant earthquakes is at least partly independent of that of regular earthquakes, allowing great and giant earthquakes to occur in both seismically active and quiet regions. In order to unravel the emergence of exceptionally large earthquakes in these settings, the underlying physical mechanisms of fault rock deformation need to be closely considered.

A microphysically based approach for earthquake modelling

The seismic cycle behaviour of (heterogeneous) faults has been explored in numerical studies[19–22], most commonly employing the rate-and-state friction[23] (RSF) formulation as a description for the time- and velocity-dependence of fault strength (see Supplementary Information S1). While the classical RSF framework is originally motivated by laboratory observations[24], it is empirical in nature, and so provides limited physical basis for the extrapolation of laboratory results to natural scales and conditions. Most importantly, the RSF model parameters are typically assumed to be independent of fault slip velocity, whereas much laboratory evidence suggests a more complex velocity-dependence of friction[25–29]. Since the fault slip velocity likely varies by over 10 orders of magnitude over the course of a seismic cycle, the assumption of constant values of the RSF constitutive parameters greatly impacts the transient slip and nucleation behaviour, as seen in seismic cycle simulations[30].

As an alternative approach, microphysical models allow for an interpretation of their parameters in terms of thermodynamic or material quantities, such as temperature, fault gouge nominal grain size, or solubility of the solid phase[31,32]. This facilitates the generalisation of complex laboratory behaviour, and the extrapolation of laboratory results to natural scales and conditions with an independent assessment of the validity of the model outcomes. Most commonly, microphysical descriptions of (steady-state) fault rheology are based on plastic creep of contact asperities between bare rock interfaces, motivated by metallurgical and tribological studies of friction of metals (e.g. refs[33–35]; Supplementary Information S2). Such models do not however fully acknowledge the complex granular dynamics of fault gouges and corresponding deformation mechanisms observed in laboratory experiments and in field studies (see Supplementary Information S3). In this study, we employ the *Chen-Niemeijer-Spiers* (CNS) model[31,36], which specifically considers the deformation of fault gouges, and is seated on laboratory and field observations. Previous work[30] has demonstrated how the implementation of the CNS model into the seismic cycle simulator QDYN[37], is capable of producing a range of fault slip behaviours previously ascribed only to rate-and-state friction, while maintaining a clear physical interpretation. In its essence, the CNS microphysical model considers the interplay between a time-dependent compaction mechanism (pressure solution creep), and dilatant granular flow (see Methods). Both these micro-mechanisms have been identified to be highly relevant for fault rock deformation at seismogenic zone conditions[29,38–42]. Because the microphysical principles for the CNS model are based on a wide range of laboratory[27,31,36] and field[43,44] observations, the model outcomes are readily understood in terms of micro-scale observable quantities.

By using a microphysical model for describing the fault rheology, one can readily incorporate field and laboratory observations into a numerical seismic cycle simulator [30]. Following numerous field studies of exhumed fault zones, we distinguish between two types of fault rock (Fig. 1 and Supplementary Information S3): a phyllite-mylonite matrix deforming predominantly by pressure solution creep, and gouge derived from "competent" lenses (competence defined at the imposed strain rate) that exhibits both pressure solution creep and granular flow. In analogy to seismogenic asperities identified by seismological studies, we refer to fault segments associated with competent lenses as asperities. These asperities obey a fractal distribution in size and separation distance (c.f. Fagereng [38]), adding to the complexity of heterogeneous faults.

In the CNS model formulation, both types of fault rock are governed by the same micro-scale mechanisms. The compositional distinction between the two types is made through a contrast in pressure solution kinetics, with the matrix exhibiting faster pressure solution kinetics than the asperities (Fig. 1b). At steady-state deformation, under the imposed fault zone conditions (effective normal stress $\sigma = 50\,\mathrm{MPa}$, far-field driving velocity $V_{imp} = 10^{-9}\,\mathrm{m/s}$, and temperature $T = 250\,^{\circ}\mathrm{C}$), the matrix deforms predominantly by velocity-strengthening ductile creep, whereas the asperities deform by parallel operation of pressure solution and granular flow, producing velocity-weakening behaviour [36]. However, in the seismic cycle simulations deformation occurs under non-steady state conditions, resulting in a spectrum of fault slip transients [30] governed by the rheological model. Following the procedure described in the Methods section, we simulate 2000 years of slip along the strike of a heterogeneous, one-dimensional periodic fault, with an along-strike length of 16 km (Fig. 1a), and investigate emergent transient slip features. Although the dimensions of the model fault are smaller than those typical for megathrusts, the outcomes of the numerical simulations are interpreted in a general framework suitable for up-scaling.

Emergence of giant earthquakes

Slip distribution maps for all 10 simulations are given in Supplementary Information S4. Examples of characteristic fault slip behaviour produced in the simulations are given in Fig. 2a. Sections on the fault that exhibit a high asperity density display repeated seismic activity, rupturing small clusters of closely-spaced asperities in a single event. Dynamic ruptures are arrested by regions consisting predominantly of ductile matrix, so that separated clusters of asperities remain mostly isolated. Motivated by Luo & Ampuero [21], we classify this type of events as partial or P-instabilities, defined as an instability that ruptures only a portion of the entire fault. Note that, unlike Luo & Ampuero [21], P-events may encompass several (clusters) of nominally velocity-weakening asperities. The seismic character of the simulation (i.e. maximum slip velocities during P-instabilities) seems largely controlled by the fractal dimension D of the asperity size distribution: simulations with $D = 1$ (dominated by several large asperities) show P-instabilities that attain coseismic slip rates, whereas simulations with $D = 2$ (dominated by numerous small asperities) only exhibit aseismic P-instabilities in the form of small slow slip events, consistent with geological observations [38].

In addition to these P-events, the fault occasionally hosts seismic events that rupture the full extent of the fault, reaching coseismic slip velocities even in regions dominated by ductile matrix. This second class of seismic events is referred to as ("total") T-instabilities. The occurrence of T-events is not restricted to simulations with seismic P-instabilities, as T-instabilities are also produced in simulations that otherwise only exhibit small slow slip events (which would likely remain undetected by surface monitoring stations). Aside from the seismic character of the model fault, the value of D also affects the style of nucleation[45] of the T-instabilities, with a cascade-up mode of nucleation observed in simulations with $D = 1$, and a preslip (or "own nucleation") mode observed in simulations with $D = 2$ (see Fig. 2a).

Extending these observations to natural fault zones, one can draw an analogy between P-events, being controlled by a local asperity distribution of nominally velocity-weakening material, and regular natural earthquakes. The T-instabilities generated in the simulations may find their natural counterpart in multi-segment ruptures and anomalously large events ($M_w > 9$), as appearing in palaeoseismic records[5,6]. It is most striking that simulations that are otherwise seismically quiet are also capable of generating T-instabilities. This shows that the mechanisms and conditions for generating T-events are different from those for P-events.

Microphysical mechanisms behind giant earthquakes

More insight into the emergence of T-instabilities is gained by considering the time-evolution of average fault stress (Fig. 2b). In simulations that exhibit a fractal dimension $D = 1$, the average shear stress supported by the asperities remains roughly constant over time, whereas the average stress on the matrix increases between subsequent T-instabilities, so that the nett fault stress increases over time. At a critical value of stress, a T-instability is generated. In the simulations with $D = 2$, the stress is more homogeneously distributed, and the stress supported by both the asperities and the matrix segments follows a similar upward trajectory, until a critical stress is reached and a T-instability nucleates.

The occurrence of a fault-spanning instability at a critical stress level can now be explained by a rheological transition predicted by the CNS model, and is illustrated in Fig. 3. At a given moment in time early in a T-cycle, a segment of ductile matrix is deforming by steady-state, non-dilatant pressure solution creep (point 1 in Fig. 3). By continuous tectonic loading and non-uniform fault slip, the average stress supported by the matrix increases over time (point 2). The kinetics of pressure solution assigned to the matrix segments are such that at steady-state (i.e. at the far-field driving velocity), the matrix can accommodate the imposed strain rate entirely by ductile creep. In the absence of interactions with the asperities on the fault, the matrix would remain nominally stable (see inset in Fig. 3). However, stress perturbations resulting from mechanical interaction with the asperities may raise the stress acting on a given matrix segment up to a critical value that marks the onset of dilatant granular flow (point 3 in Fig. 3). If a sufficient volume of matrix is critically stressed, a T-instability is triggered in which both the asperities and the matrix segments enter the unstable granular flow regime (point 4). A fault-spanning rupture then results as the entire fault has become unstable.

It is noteworthy that this rheological transition predicted by the CNS microphysical model has been observed in various materials in laboratory experiments[27–29,46]. This transition is commonly known as the brittle-ductile[47], or flow-to-friction[48] transition. The outcomes of the numerical simulations are therefore not a mere peculiarity unique to the adopted fault rheology, and it is expected that models that feature such brittle-ductile transition (e.g. Den Hartog & Spiers[32] and Noda & Shimamoto[49]) will display similar behaviour. However, microphysical models from which the brittle-ductile transition naturally emerges are more appealing that purely empirical flow-to-friction laws, as they can be extrapolated based on measurable material properties, and thereby have stronger predictive capabilities.

Discussion and future perspectives

It has been proposed[9,10,50] that giant earthquakes are a consequence of the conservation of seismic moment, which requires that the long-term slip budget be closed. However, the exact mechanism by which this occurs has yet to be elucidated. The stress-driven transition from non-dilatant to dilatant deformation provides a plausible mechanism for conserving seismic moment on long (centennial to millenary) time-scales. Furthermore, this mechanism exhibits two additional characteristics that are in line with (palaeo)seismological studies: firstly, T-instabilities have been observed in the simulations to occur both on seismically active and quiet faults, in agreement with natural observations from e.g. the regions of Cascadia, Andaman, Japan Trench, and Sumatra[5,8,18]. Secondly, the observed T-instabilities do not occur randomly in time, but are instead time-predictable depending on the long-term rate of seismic moment accumulation and release[10].

Lastly, the rheological transition from non-dilatant to dilatant deformation, as demonstrated experimentally and as embodied by the CNS model, is inherently absent in the classical rate-and-state friction formulations. By adopting a rheological model that is based on micro-scale physical processes, new model features may arise that can be directly compared with laboratory, geological, and (palaeo)seismological observations. In this way, future seismic hazard assessments can be complemented with physical considerations, in addition to existing statistical inferences.

References

[1] Benedetti, L. *et al.* Earthquake synchrony and clustering on Fucino faults (Central Italy) as revealed from in situ 36 Cl exposure dating. *Journal of Geophysical Research: Solid Earth* **118**, 4948–4974 (2013).

[2] Philibosian, B. *et al.* Earthquake supercycles on the Mentawai segment of the Sunda megathrust in the seventeenth century and earlier. *Journal of Geophysical Research: Solid Earth* **122**, 642–676 (2017).

[3] Ratzov, G. *et al.* Holocene turbidites record earthquake supercycles at a slow-rate plate boundary. *Geology* **43**, 331–334 (2015).

[4] Sieh, K. *et al.* Earthquake Supercycles Inferred from Sea-Level Changes Recorded in the Corals of West Sumatra. *Science* **322**, 1674–1678 (2008).

[5] Goldfinger, C. *et al.* Turbidite Event History — Methods and Implications for Holocene Paleoseismicity of the Cascadia Subduction Zone. *U.S. Geological Survey Professional Paper 1661-F* 170 (2012).

[6] Goldfinger, C., Ikeda, Y., Yeats, R. S. & Ren, J. Superquakes and Supercycles. *Seismological Research Letters* **84**, 24–32 (2013).

[7] Mannen, K. *et al.* History of ancient megathrust earthquakes beneath metropolitan Tokyo inferred from coastal lowland deposits. *Sedimentary Geology* (2017).

[8] Satake, K. Geological and historical evidence of irregular recurrent earthquakes in Japan. *Philosophical Transactions of the Royal Society A: Mathematical, Physical and Engineering Sciences* **373**, 20140375 (2015).

[9] Stevens, V. L. & Avouac, J.-P. Millenary M w > 9.0 earthquakes required by geodetic strain in the Himalaya. *Geophysical Research Letters* **43**, 1118–1123 (2016).

[10] Satake, K. & Fujii, Y. Review: Source Models of the 2011 Tohoku Earthquake and Long-Term Forecast of Large Earthquakes. *Journal of Disaster Research* **9**, 272–280 (2014).

[11] Ruff, L. & Kanamori, H. Seismicity and the subduction process. *Physics of the Earth and Planetary Interiors* **23**, 240–252 (1980).

[12] Satake, K. & Atwater, B. F. Long-Term Perspectives on Giant Earthquakes and Tsunamis at Subduction Zones *. *Annu. Rev. Earth Planet. Sci* **35**, 349–74 (2007).

[13] Kagan, Y. Y. Seismic moment-frequency relation for shallow earthquakes: Regional comparison. *Journal of Geophysical Research: Solid Earth* **102**, 2835–2852 (1997).

[14] McCaffrey, R. Global frequency of magnitude 9 earthquakes. *Geology* **36**, 263 (2008).

[15] Weng, H. & Yang, H. Seismogenic width controls aspect ratios of earthquake ruptures. *Geophysical Research Letters* **44**, 2725–2732 (2017).

[16] Ohta, Y., Freymueller, J., Hreinsdottir, S. & Suito, H. A large slow slip event and the depth of the seismogenic zone in the south central Alaska subduction zone. *Earth and Planetary Science Letters* **247**, 108–116 (2006).

[17] Gomberg, J. Slow-slip phenomena in Cascadia from 2007 and beyond: A review. *Geological Society of America Bulletin* **122**, 963–978 (2010).

[18] Ide, S. The proportionality between relative plate velocity and seismicity in subduction zones. *Nature Geoscience* **6**, 780–784 (2013).

[19] Hillers, G., Ben-Zion, Y. & Mai, P. M. Seismicity on a fault controlled by rate- and state-dependent friction with spatial variations of the critical slip distance. *Journal of Geophysical Research* **111**, B01403 (2006).

[20] Kaneko, Y., Avouac, J. & Lapusta, N. Towards inferring earthquake patterns from geodetic observations of interseismic coupling. *Nature Geoscience* **3**, 363–369 (2010).

[21] Luo, Y. & Ampuero, J.-P. Stability and effective friction of faults with heterogeneous friction properties and fluid pressure. *Tectonophysics* (2017).

[22] Tse, S. T. & Rice, J. R. Crustal earthquake instability in relation to the depth variation of frictional slip properties. *Journal of Geophysical Research* **91**, 9452 (1986).

[23] Dieterich, J. H. Modeling of rock friction: 1. Experimental results and constitutive equations. *Journal of Geophysical Research* **84**, 2161 (1979).

[24] Dieterich, J. H. Time-dependent friction in rocks. *Journal of Geophysical Research* **77**, 3690–3697 (1972).

[25] Carpenter, B., Collettini, C., Viti, C. & Cavallo, A. The influence of normal stress and sliding velocity on the frictional behaviour of calcite at room temperature: insights from laboratory experiments and microstructural observations. *Geophysical Journal International* **205**, 548–561 (2016).

[26] den Hartog, S., Niemeijer, A. & Spiers, C. New constraints on megathrust slip stability under subduction zone P–T conditions. *Earth and Planetary Science Letters* **353-354**, 240–252 (2012).

[27] Niemeijer, A. R. & Spiers, C. J. Velocity dependence of strength and healing behaviour in simulated phyllosilicate-bearing fault gouge. *Tectonophysics* **427**, 231–253 (2006).

[28] Shimamoto, T. Transition Between Frictional Slip and Ductile Flow for Halite Shear Zones at Room Temperature. *Science* **231**, 711–714 (1986).

[29] Verberne, B. A. *et al.* Microscale cavitation as a mechanism for nucleating earthquakes at the base of the seismogenic zone. *Nature Communications* **8**, 1645 (2017).

[30] van den Ende, M. P. A., Chen, J., Ampuero, J.-P. & Niemeijer, A. R. A direct comparison between rate-and-state friction and microphysical models, based on earthquake cycle simulations. *Tectonophysics* (2017).

[31] Chen, J. & Spiers, C. J. Rate and state frictional and healing behavior of carbonate fault gouge explained using microphysical model. *Journal of Geophysical Research: Solid Earth* 1–42 (2016).

[32] den Hartog, S. A. M. & Spiers, C. J. A microphysical model for fault gouge friction applied to subduction megathrusts. *Journal of Geophysical Research: Solid Earth* **119**, 1510–1529 (2014).

[33] Brechet, Y. & Estrin, Y. The effect of strain rate sensitivity on dynamic friction of metals. *Scripta metallurgica et materialia* **30**, 1449–1454 (1994).

[34] Perfettini, H. & Molinari, A. A Micromechanical Model of Rate and State Friction: 1. Static and Dynamic Sliding. *Journal of Geophysical Research: Solid Earth* (2017).

[35] Aharonov, E. & Scholz, C. H. A physics-based rock-friction constitutive law: steady-state friction. *Journal of Geophysical Research: Solid Earth* (2017).

[36] Niemeijer, A. R. & Spiers, C. J. A microphysical model for strong velocity weakening in phyllosilicate-bearing fault gouges. *Journal of Geophysical Research* **112**, B10405 (2007).

[37] Luo, Y., Ampuero, J.-P., Galvez, P., Van den Ende, M. & Idini, B. QDYN: a Quasi-DYNamic earthquake simulator (v1.1) (2017).

[38] Fagereng, Å. Geology of the seismogenic subduction thrust interface. *Geological Society, London, Special Publications* **359**, 55–76 (2011).

[39] Holdsworth, R. *et al.* Fault rocks from the SAFOD core samples: Implications for weakening at shallow depths along the San Andreas Fault, California. *Journal of Structural Geology* **33**, 132–144 (2011).

[40] Jefferies, S. *et al.* The nature and importance of phyllonite development in crustal-scale fault cores: an example from the Median Tectonic Line, Japan. *Journal of Structural Geology* **28**, 220–235 (2006).

[41] Smeraglia, L. *et al.* Microstructural evidence for seismic and aseismic slips along clay-bearing, carbonate faults. *Journal of Geophysical Research: Solid Earth* (2017).

[42] Chester, F. M. & Higgs, N. G. Multimechanism friction constitutive model for ultrafine quartz gouge at hypocentral conditions. *Journal of Geophysical Research: Solid Earth* **97**, 1859–1870 (1992).

[43] Niemeijer, A. R. & Vissers, R. L. Earthquake rupture propagation inferred from the spatial distribution of fault rock frictional properties. *Earth and Planetary Science Letters* **396**, 154–164 (2014).

[44] Rowe, C. D., Meneghini, F. & Moore, J. C. Textural record of the seismic cycle: strain-rate variation in an ancient subduction thrust. *Geological Society, London, Special Publications* **359**, 77–95 (2011).

[45] Ellsworth, W. L. & Beroza, G. C. Seismic Evidence for an Earthquake Nucleation Phase. *Science* **268**, 851–855 (1995).

[46] Reinen, L. A., Tullis, T. E. & Weeks, J. D. Two-mechanism model for frictional sliding of serpentinite. *Geophysical Research Letters* **19**, 1535–1538 (1992).

[47] Sibson, R. H. Fault zone models, heat flow, and the depth distribution of earthquakes in the continental crust of the United States. *Bulletin of the Seismological Society of America* **72**, 151–163 (1982).

[48] Noda, H. & Shimamoto, T. Transient behavior and stability analyses of halite shear zones with an empirical rate-and-state friction to flow law. *Journal of Structural Geology* **38**, 234–242 (2012).

[49] Shimamoto, T. & Noda, H. A friction to flow constitutive law and its application to a 2-D modeling of earthquakes. *Journal of Geophysical Research: Solid Earth* **119**, 8089–8106 (2014).

[50] Kagan, Y. Y. & Jackson, D. D. Tohoku Earthquake: A Surprise? *Bulletin of the Seismological Society of America* **103**, 1181–1194 (2013).

Acknowledgements

MvdE thanks Å. Fagereng for sharing his views on fault zone structure. This project is supported by the European Research Council (ERC), grant no. 335915, and by the NWO Vidi-grant 854.12.001 awarded to A.R. Niemeijer. JPA acknowledges supplemental funding to NSF CAREER grant EAR-1151926 for research opportunities in Europe.

Author contributions

All authors contributed in the design of the study. MvdE carried out the numerical simulations and prepared the manuscript. All authors discussed the model results and interpretations, and commented on the manuscript.

Competing financial interests

The authors declare no competing financial interests.

Methods

Description of the microphysical model. The derivation of the CNS model, the comparison with classical rate-and-state friction, and its implementation into QDYN are described in detail in refs [1–5]. Some key concepts of this model are recited here.

The CNS model geometry is based on the microstructural observations provided by ref. 27, and considers a granular gouge layer of uniform thickness h, characterised by a nominal grain size d and porosity ϕ. A representative volume element is subjected to an effective normal stress σ and deformation rate V_{imp}, which is accommodated internally by parallel operation of granular flow (grain rolling and sliding), and one or more thermally-activated, time-dependent deformation mechanisms. Following previous work [1–3] and based on the observations summarised in Supplementary Information S3, we take intergranular pressure solution as the sole time-dependent mechanism, ignoring other mechanisms such as stress corrosion cracking [6,7]. The constitutive relation for the rheology of the fault then results from the individual constitutive relations for granular flow and pressure solution, which are dependent on the instantaneous state of stress and gouge porosity.

For intergranular pressure solution, the flow law for dissolution controlled pressure solution creep is given as [8,9]:

$$\dot{\gamma}_{ps} = A\frac{I_s\Omega}{RT}\frac{\tau}{d}f_1(\phi) \tag{1a}$$

$$\dot{\varepsilon}_{ps} = A\frac{I_s\Omega}{RT}\frac{\sigma}{d}f_2(\phi) \tag{1b}$$

Here, $\dot{\gamma}_{ps}$ and $\dot{\varepsilon}_{ps}$ are the strain rates in the fault tangential and normal directions, respectively, A is a geometric factor accounting for the grain shape, I_s is the dissolution rate constant, Ω is the molar volume, R is the universal gas constant, T is the absolute temperature, and τ and σ are the macroscopic shear and effective normal stress, respectively. The evolution of the grain-grain contact area (and grain contact stress) with porosity ϕ is described by the porosity function $f_i(\phi)$ [10]. For dissolution controlled pressure solution creep, this function takes the following form [3,9]:

$$f_1(\phi) = \frac{\phi_c}{\phi_c - \phi} \tag{2a}$$

$$f_2(\phi) = \frac{\phi - \phi_0}{\phi_c - \phi} \tag{2b}$$

where ϕ_0 is a lower cut-off porosity corresponding to the percolation threshold for an interconnected pore network of $3\,\%$ [11], and ϕ_c is the maximum attainable porosity of a purely dilatant gouge material, referred to here as the 'critical state' porosity [1,12]. Typically, a porosity function similar to $f_1(\phi)$ is used in analytical models for intergranular pressure solution that employ a porosity function [9,10]. However, in laboratory compaction test it has been observed that microphysical model predictions for compaction by pressure solution overestimate experimentally measured strain rates at low porosities ($< 20\,\%$), sometimes by several orders of magnitude [8]. While the physical mechanisms behind this discrepancy are yet to be fully identified, the trends in the experimental data can be approximated by the modified porosity function $f_2(\phi)$, which asymptotically reduces $\dot{\varepsilon}_{ps}$ to zero for $\phi \rightarrow \phi_0$. Furthermore, this ensures that $\phi > \phi_0$ at all times, preventing negative porosities that are physically unrealistic. By contrast, shear creep accommodated by pressure solution does not involve volume changes (i.e. porosity reduction), so it is expected that $\dot{\gamma}_{ps} > 0$ even for $\phi = \phi_0$. A functional form like $f_1(\phi)$ is therefore more likely to describe shear creep by pressure solution, as is adopted for this study.

The constitutive relations for granular flow have been derived as[2]:

$$\dot{\gamma}_{gr} = \dot{\gamma}_{gr}^{*} \exp\left(\frac{\tau\left[1 - \tilde{\mu}^{*}\tan\psi\right] - \sigma\left[\tilde{\mu}^{*} + \tan\psi\right]}{\tilde{a}\left[\sigma + \tau\tan\psi\right]}\right) \tag{3a}$$

$$\dot{\varepsilon}_{gr} = -\tan\psi\dot{\gamma}_{gr} \tag{3b}$$

In these relations, $\dot{\gamma}_{gr}$ and $\dot{\varepsilon}_{gr}$ denote the granular flow strain rates tangential and normal to the fault plain, respectively, and $\tan\psi$ denotes the average grain-grain dilatation angle, which can be written as $\tan\psi = 2H\left(\phi_c - \phi\right)$, where H is a geometric constant of order 1[1,12]. The microscopic coefficient of friction of grain-grain contacts is given by ref. 2 as $\tilde{\mu} = \tilde{\mu}^{*} + \tilde{a}\ln\left(\dot{\gamma}_{gr}/\dot{\gamma}_{gr}^{*}\right)$, $\tilde{\mu}^{*}$ being a reference value of $\tilde{\mu}$ evaluated at $\dot{\gamma}_{gr}^{*}$, and $\tilde{a}$ being the coefficient of logarithmic rate-dependence of $\tilde{\mu}$.

With the above constitutive relations for the relevant deformation mechanisms, the evolution of the macroscopic shear stress and gouge porosity of a zero-dimensional (spring-block) fault can be expressed in the following set of differential equations[2]:

$$\frac{\mathrm{d}\tau}{\mathrm{d}t} = k\left(V_{imp} - h\left[\dot{\gamma}_{gr} + \dot{\gamma}_{ps}\right]\right) \tag{4a}$$

$$\frac{\mathrm{d}\phi}{\mathrm{d}t} = -\left(1 - \phi\right)\left(\dot{\varepsilon}_{gr} + \dot{\varepsilon}_{ps}\right) \tag{4b}$$

in which k is the effective shear stiffness (units: Pa m^{-1}) of the fault. The instantaneous fault slip velocity V is obtained from the addition of the strain rates of granular flow and pressure solution (i.e. $V = h\left[\dot{\gamma}_{gr} + \dot{\gamma}_{ps}\right]$).

One important characteristic to note, is that the steady-state velocity-dependence of friction, i.e. a material being velocity-strengthening or -weakening, changes with velocity (see Fig. 1b). As a result, classical rate-and-state friction is only comparable to the CNS model near steady-state conditions[5]. With increasing departure from steady-state, both model frameworks predict different frictional behaviour, as is notably seen in seismic cycle simulations[3].

Description of the boundary element method. To model spatio-temporal variations of fault slip, we employ the boundary element code QDYN[13]. This seismic cycle simulator originally utilises rate-and-state friction to describe the model fault rheology, but it has been extended[3] to include the CNS microphysical model as described above in above. Regardless of the underlying rheological model, the shear stress at point i on the fault is obtained using the quasi-dynamic approximation[14]:

$$\tau_i(t) = -K_{ij}\left[d_j(t) - d_{imp}\right] - \eta V_i(t) \tag{5}$$

Here, K_{ij} is a stress transfer kernel whose coefficients represent the shear stress induced on the i-th fault element by unitary slip on the j-th fault element, d_j is the total fault slip on the j-th fault element, and d_{imp} is the far-field displacement, accumulating as $d_{imp} = V_{imp} \times t$. Radiation damping due to seismic wave radiation normal to the fault plane is accounted for by the last term on the right-hand side, in which the damping factor η assumes a value of $G/2c_s$, with G being the shear modulus of the homogeneous elastic medium, and c_s the shear wave speed[14]. The stress transfer kernel K_{ij} is computed using a "2.5D" approximation for infinite one-dimensional faults embedded in two-dimensional homogeneous media (see ref. 21), and fault stresses are obtained via the spectral approach in finite-size domains[15]. For numerical implementation, Eqn. 5 is differentiated with respect to time to give:

$$\frac{\mathrm{d}\tau_i}{\mathrm{d}t} = -K_{ij}\left[V_j(t) - V_{imp}\right] - \eta \frac{\mathrm{d}V_i(t)}{\mathrm{d}t} \tag{6}$$

The fault slip velocity $V(t)$ is obtained as a function of stress and porosity as $V(\tau, \sigma, \phi) = h\left[\dot{\gamma}_{gr}(\tau, \sigma, \phi) + \dot{\gamma}_{ps}(\tau, \phi)\right]$. The acceleration term on right hand side of Eqn. (6) is then decomposed in its partial derivatives as:

$$\frac{\mathrm{d}V}{\mathrm{d}t} = \frac{\partial V}{\partial \tau}\frac{\mathrm{d}\tau}{\mathrm{d}t} + \frac{\partial V}{\partial \phi}\frac{\mathrm{d}\phi}{\mathrm{d}t} \tag{7a}$$

$$\frac{\partial V}{\partial \tau} = h\left(A\frac{I_s\Omega}{dRT}f_1(\phi) + \dot{\gamma}_{gr}\left[\frac{1-\tilde{\mu}\tan\psi}{\tilde{a}\left(\sigma + \tau\tan\psi\right)}\right]\right) \tag{7b}$$

$$\frac{\partial V}{\partial \phi} = h\left(\frac{\dot{\gamma}_{ps}}{\phi_c - \phi} + \dot{\gamma}_{gr}\left[\frac{2H\left(\sigma + \tilde{\mu}\tau\right)}{\tilde{a}\left(\sigma + \tau\tan\psi\right)}\right]\right) \tag{7c}$$

Note that these partial derivatives are given specifically for the assumed porosity functions (Eqn. (2)). Substitution of (7) into (6), and rearrangement gives:

$$\frac{\mathrm{d}\tau_i}{\mathrm{d}t} = \frac{-K_{ij}\left[V_j - V_{imp}\right] - \eta\frac{\partial V_i}{\partial \phi}\frac{\mathrm{d}\phi_i}{\mathrm{d}t}}{1 + \eta\frac{\partial V_i}{\partial \tau}} \tag{8a}$$

$$\frac{\mathrm{d}\phi_i}{\mathrm{d}t} = -\left(1 - \phi_i\right)\left(\dot{\varepsilon}_{gr,i} + \dot{\varepsilon}_{ps,i}\right) \tag{8b}$$

These equations are of the general form $\dot{\mathbf{X}} = \mathbf{F}(\mathbf{X}, t)$, with $\mathbf{X}(t)$ being a vector containing the collection of $\tau_i(t)$ and $\phi_i(t)$ variables on all fault elements. This system of ordinary differential equations is solved by the $4(5)^{\text{th}}$-order Runge-Kutta-Fehlberg method with adaptive time stepping[16,17].

Rendering the heterogeneous fault structure. By employing a microphysical model that contains microstructural information, one can closely relate the model fault geometry to field and laboratory observations. In this work, guided by numerous field reports, we define heterogeneity through spatial variations in pressure solution kinetics, which reflect contrasts in fault rock composition or spatial variations in strain rate. Following ref. 38, we assume that competent lenses (the asperities) obey a power-law distribution in size, i.e.:

$$F_X(x) = 1 - cx^{-D} \tag{9}$$

where F_X is the cumulative size distribution of asperity size X, D is the fractal dimension (or power-law exponent), and c is a proportionality constant. Strictly speaking, this cumulative distribution function does not exist for $D > 0$ on an infinite domain, but it can be re-defined based on a re-scaled probability density function integrated over a finite range of $0 < x_{min} \leq X \leq x_{max}$ and $D \neq 0$, which yields:

$$f'_X(x) = \frac{-Dx^{-D-1}}{x_{max}^{-D} - x_{min}^{-D}} \tag{10a}$$

$$F'_X(x) = \int_{x_{min}}^{x} f'_X(x)\mathrm{d}x = \frac{x^{-D} - x_{min}^{-D}}{x_{max}^{-D} - x_{min}^{-D}} \tag{10b}$$

In accordance with the above relations, the realisation of the asperity size distribution x can be generated from a uniform variate $\widehat{X}$ as:

$$x = \left(x_{min}^{-D} + \left[x_{max}^{-D} - x_{min}^{-D}\right]\widehat{X}\right)^{-1/D} \tag{11}$$

The procedure to render a fault with the desired statistical properties is then as follows:

1. First, the discrete asperity size distribution x_i is realised in accordance with Eqn. (11), with x_{min} corresponding to twice the fault element size, and $x_{max} = L$. Between simulations, D is systematically varied between 1 and 2, following the phacoid fractal dimensions reported by ref. 38;

2. Next, a second size distribution (y_i) is realised that represents the spacing between neighbouring asperities, assuming that the "gaps" between asperities obey the same power-law distribution;

3. In order to obtain the desired asperity occupation ratio f, x_i is multiplied by $f/(1-f)$ (i.e. the ratio of total asperity length over total matrix length) before being combined in an arrangement with y_i;

4. The spatial distribution of Z_{ps} for the asperities and the matrix is then sampled from a piece-wise alternating arrangement of x_i and y_i, respectively, where i ranges from 1 to N, so that $\sum_{i=1}^{N}(x_i + y_i) \geq L$. In other words, the spatial layout of the fault follows an arrangement $x_1, y_1, x_2, y_2, ..., x_N, y_N$;

Owing to the fault's finite size, stochastic noise causes some variability in the statistical properties of the fault geometry, e.g. by randomly introducing one excessively large asperity, which skews the asperity size distribution. To prevent this, we compare each realised asperity size distribution with the expected distribution (Eqn. (10b)), and the realised value of f with the one that is requested. For large ($> 5\,\%$) deviations of the size distribution and f from the expected values, the rendered fault structure is rejected and a new one generated.

From the above procedure, we obtain a fault structure that is consistent with our interpretation of the field observations summarised in Supplementary Information S3 (see also Fig. 1). This fault geometry is projected onto a one-dimensional periodic fault, and the fault is subjected to down-dip conditions of $V_{imp} = 10^{-9}$ m s^{-1} and $\sigma = 50\,$MPa. For the kinetics of pressure solution Z_{ps} defining the asperity and the matrix, we adopt values of 5×10^{-16} and 3×10^{-15} Pa^{-1} s^{-1}. A value of $Z_{ps} = 3 \times 10^{-15}$ Pa^{-1} s^{-1} corresponds to theoretical estimates of Z_{ps} for monomineralic quartz at 250 °C and a grain size of 5 μm[8]. The simulation is then run for at least 2,000 years.

References

[1] Niemeijer, A. R. & Spiers, C. J. A microphysical model for strong velocity weakening in phyllosilicate-bearing fault gouges. *Journal of Geophysical Research* **112**, B10405 (2007).

[2] Chen, J. & Spiers, C. J. Rate and state frictional and healing behavior of carbonate fault gouge explained using microphysical model. *Journal of Geophysical Research: Solid Earth* 1–42 (2016).

[3] van den Ende, M. P. A., Chen, J., Ampuero, J.-P. & Niemeijer, A. R. A direct comparison between rate-and-state friction and microphysical models, based on earthquake cycle simulations. *Tectonophysics* (2017).

[4] Chen, J. & Niemeijer, A. R. Seismogenic Potential of a Gouge-filled Fault and the Criterion for Its Slip Stability: Constraints From a Microphysical Model. *Journal of Geophysical Research: Solid Earth* **122**, 9658–9688 (2017).

[5] Chen, J., Niemeijer, A. R. & Spiers, C. J. Microphysically derived expressions for rate-and-state friction parameters, a , b , and D c. *Journal of Geophysical Research: Solid Earth* (2017).

[6] Atkinson, B. K. Subcritical crack growth in geological materials. *Journal of Geophysical Research* **89**, 4077 (1984).

[7] Brantut, N., Heap, M. J., Meredith, P. G. & Baud, P. Time-dependent cracking and brittle creep in crustal rocks: A review. *Journal of Structural Geology* **52**, 17–43 (2013).

[8] Niemeijer, A. R., Spiers, C. J. & Bos, B. Compaction creep of quartz sand at 400-600C: experimental evidence for dissolution-controlled pressure solution. *Earth and Planetary Science Letters* **195**, 261–275 (2002).

[9] Pluymakers, A. M. H. & Spiers, C. J. Compaction creep of simulated anhydrite fault gouge by pressure solution: theory v. experiments and implications for fault sealing. *Geological Society, London, Special Publications* **409**, 107–124 (2014).

[10] Spiers, C. J., De Meer, S., Niemeijer, A. R. & Zhang, X. Kinetics of rock deformation by pressure solution and the role of thin aqueous films. In Nakashima, S., Spiers, C. J., Mercury, L., Fenter, P. A. & Hochella, M. F. J. (eds.) *Physicochemistry of Water in Geological and Biological Systems*, 129–158 (Universal Academy Press, Tokyo, 2004).

[11] van der Marck, S. C. Network Approach to Void Percolation in a Pack of Unequal Spheres. *Physical Review Letters* **77**, 1785–1788 (1996).

[12] Paterson, M. S. A theory for granular flow accommodated by material transfer via an intergranular fluid. *Tectonophysics* **245**, 135–151 (1995).

[13] Luo, Y., Ampuero, J.-P., Galvez, P., Van den Ende, M. & Idini, B. QDYN: a Quasi-DYNamic earthquake simulator (v1.1) (2017).

[14] Rice, J. R. Spatio-temporal complexity of slip on a fault. *Journal of Geophysical Research* **98**, 9885 (1993).

[15] Cochard, A. & Rice, J. R. A spectral method for numerical elastodynamic fracture analysis without spatial replication of the rupture event. *Journal of the Mechanics and Physics of Solids* **45**, 1393–1418 (1997).

[16] Fehlberg, E. Low-Order Classical Runge-Kutta Formulas with Step-Size Control and Their Application to some Heat-Transfer Problems. *NASA Technical Report* **315** (1969).

[17] Shampine, L. F., Watts, H. A. & Davenport, S. M. Solving Nonstiff Ordinary Differential Equations - The State of the Art. *SIAM Review* **18**, 376–411 (1976).

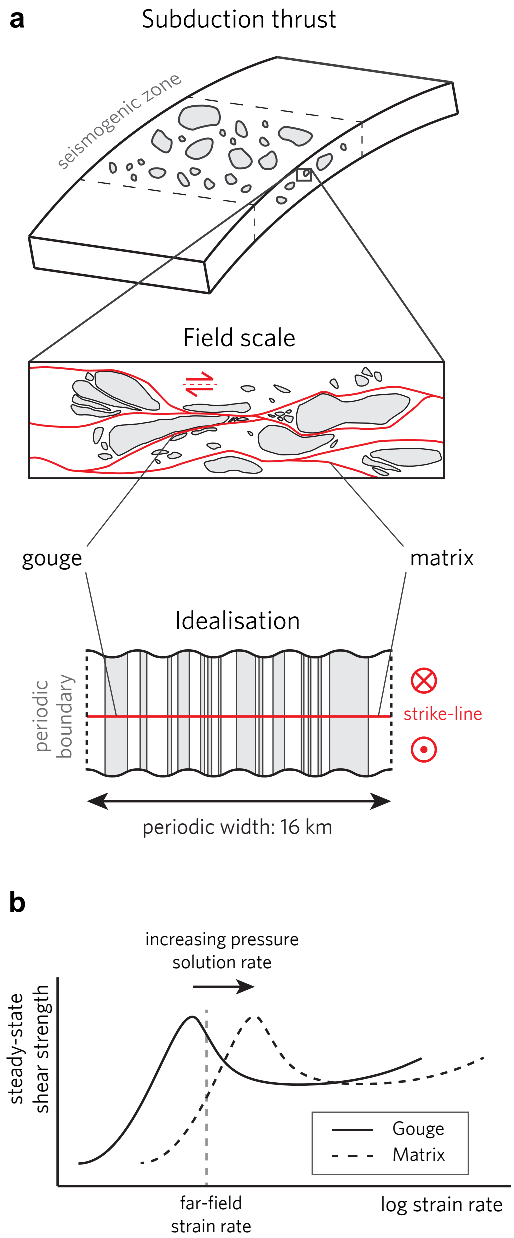

Figure 1 Properties of the model fault. **a**, Idealisation of the envisioned fault geometry, after Fagereng[38]. **b**, Schematic diagram of the steady-state shear strength versus strain rate, as predicted by the CNS microphysical model. The compositional variation along the fault is reflected by a contrast in pressure solution kinetics, causing a relative shift of the steady-state strength curves.

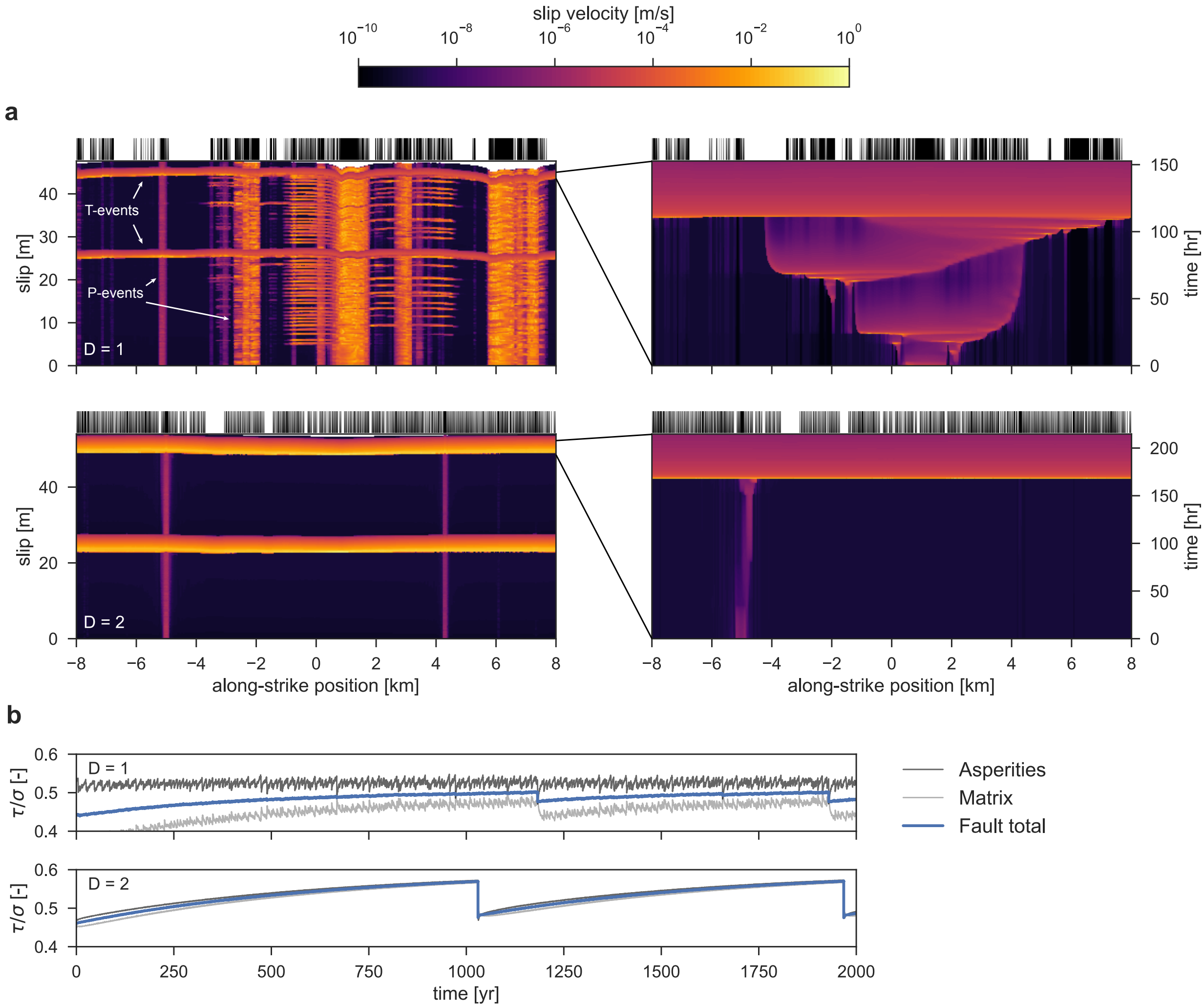

Figure 2 **Examples of model fault behaviour.** **a**, Spatio-temporal distribution of fault slip velocity (left panels) and nucleation of the last T-instability in each simulation (right panels). The fractal dimension D is as indicated. P-instabilities are identified as small 'hot' regions that span only a portion of the fault, whereas T-instabilities span the entire fault. For reference, the seismogenic asperity distribution is indicated by the black bars at the top of each panel. Simulations with $D = 1$ show numerous regular earthquakes controlled by the local asperity distribution, and a cascade-up style of nucleation of a T-instability. Simulations with $D = 2$ exhibits only minute slow slip events during the interseismic period of a T-event, which emerges with no precursory activity from a small nucleus. **b**, Time-series of the average stress supported by the asperities, the matrix, and the fault as a whole, for $D = 1$ and $D = 2$. A T-instability is triggered when the stress supported by the matrix reaches a critical value.

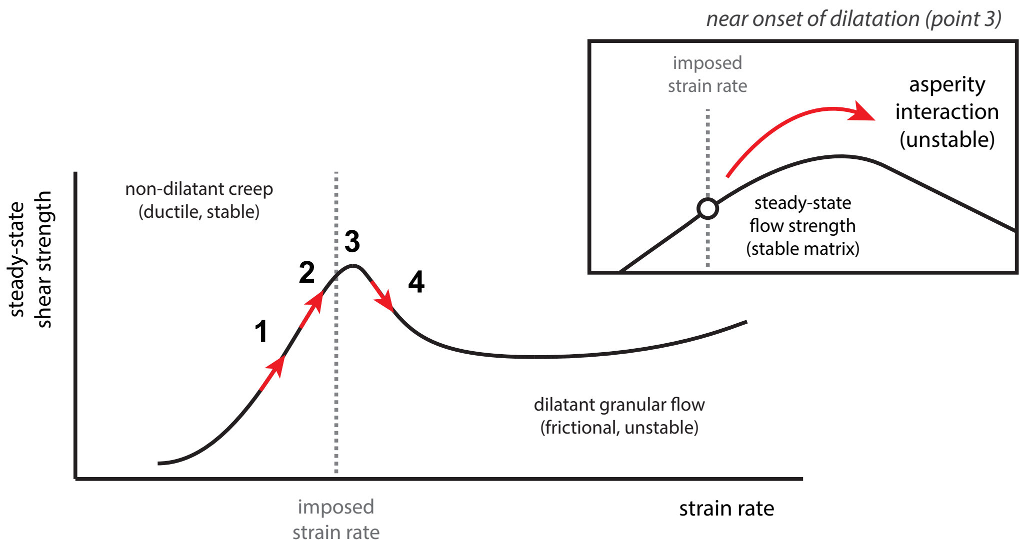

Figure 3 Synoptic overview of the nucleation process. The steady-state strength profile of the matrix, as a function of strain rate, is characterised by a transition from non-dilatant ductile creep (stable) to dilatant granular flow (unstable). At a given moment in time, the stress supported by the matrix is indicated by point 1. Due to tectonic loading and non-uniform fault slip, the stress on the matrix increases (point 2). At a critical value of stress, the matrix enters the dilatant granular flow regime, and a T-instability nucleates.